

Analytical, FEM and Experimental Study of the Influence of the Airgap Size in Different Types of Ferrite Cores

Asier Arruti¹, Francisco Jose Perez-Cebolla², Jon Anzola¹, Iosu Aizpuru¹, Mikel Mazuela¹

¹Mondragon Unibertsitatea, Mondragon, Spain

²University of Zaragoza, Zaragoza, Spain

E-Mail: aarruti@mondragon.edu, fperez@unizar.es

Acknowledgements

This research has been supported by the Department of Education of the Basque Government under the Non Doctoral Research Staff Training Program through grant PRE_2020_1_0229.

Keywords

«Flux model», «Magnetic device», «Passive component», «Permeability»

Abstract

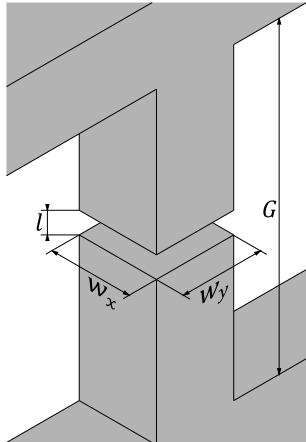
This work reviews and compares different airgap reluctance calculation approaches with experimental results, focusing on the Schwarz-Christoffel transformation. The modelling of the airgap reluctance in two dimensions is tested against FEM simulations for typical airgap geometries. Then, an approach to obtain the three-dimensional reluctance is shown, and the limited experimental data shown in previous works is expanded to validate the different airgap calculation methods in EE cores. For the case of pot cores, a geometrical transformation is proposed and validated, allowing the application of the Schwarz-Christoffel methodology to other common core geometries.

Introduction

The analysis and design of inductors is a critical task in power electronics applications. Reluctance models based on equivalent magnetic circuits have long been used for this; they are analogue to electric circuits, making them familiar to electronic engineers, and they allow for quick and easy calculations of the magnetic flux density and inductance.

When using highly permeable magnetic cores, an airgap is added to the magnetic path in the cores. This airgap has a high reluctance, so that it can be used to adjust the effective reluctance of the core, also contributing to alleviate the temperature dependency of the material and helps to avoid saturation of the magnetic core. Unfortunately, the airgap reluctance is not only the most impactful element in the reluctance model, it is also the most difficult to calculate due to the magnetic field distribution.

Various techniques have been proposed to calculate this value [1]–[8]. The simplest approach to estimate the airgap reluctance from Fig. 1 is to assume that the same magnetic field distribution of the core applies to the airgap [1]. Here, w_x and w_y are the widths of the core in the x and y directions, while l is the length of the airgap in the z direction, so that the reluctance is then (1).



$$\mathcal{R} = \frac{l}{\mu_0 w_x w_y} \quad (1)$$

Fig. 1: Visual representation of the airgap added to a magnetic material path.

Inside the core, due to the high relative permeability, practically all of the magnetic flux is confined in the magnetic area, but this is not true in the airgap, and a fringing flux appears. The existence of the fringing field increases the effective area and reduces the airgap reluctance, and thus, (1) will not give accurate results for the reluctance.

Some other approaches to estimate the airgap reluctance have been proposed. The most commonly known technique is based on increasing the cross-section as a function of the airgap [3]–[5]. In general, this is done by adding the airgap length to the widths of the cross-section, so that the airgap is then (2). To our knowledge, there is no mathematical proof of (2), and it appears to be developed based on experimental data. Similarly, the use of the correction factor F (3) is proposed in [6]–[8], which is developed based on experimental data. In this case a new variable G is introduced, defined as the winding height (Fig. 1). The correction factor F is then used to calculate the airgap reluctance as shown in (4).

$$\mathcal{R} = \frac{l}{\mu_0(w_x + l)(w_y + l)} \quad (2)$$

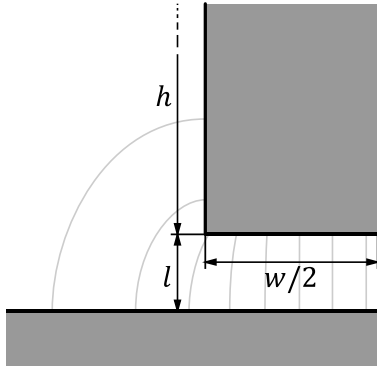
$$F = 1 + \frac{l}{\sqrt{w_x w_y}} \ln \frac{2G}{l} \quad (3)$$

$$\mathcal{R} = \frac{l}{\mu_0 w_x w_y} / F = \frac{1}{\frac{\mu_0 w_x w_y}{l} + \mu_0 \sqrt{w_x w_y} \ln \frac{2G}{l}} \quad (4)$$

Computer based numerical solutions such as finite element methods (FEM) can be used to accurately model the fringing field and resolve the airgap reluctance [9]–[11], but these approaches are much more computationally expensive. This makes them prohibitively slow to use in inductor design and optimization tools, where thousands of different cases have to be quickly analysed and compared.

Airgap calculation using the Schwarz-Christoffel transformation

Another technique for the calculation of the airgap is proposed in [12]. Unlike the previous methods, this approach uses the Schwarz-Christoffel transformation, which makes use of the analogy between the electric field and capacitance, and the magnetic field and reluctance. Note that the technicalities of the Schwarz-Christoffel transformation will not be discussed in this publication, and it will focus on the application of the base reluctance defined in [12].



$$\mathcal{R}_{base} = \frac{1}{\mu_0 \left[\frac{w}{2l} + \frac{2}{\pi} \left(1 + \ln \frac{\pi h}{4l} \right) \right]} \quad (5)$$

Fig. 2: Base reluctance based on the Schwarz-Christoffel transformation.

For the two-dimensional geometry of Fig. 2, the two-dimensional base reluctance can be defined as a function of the geometry (5). This base reluctance serves as the building block to solve more complex two-dimensional cases. Although the approach from [12] is confined to two-dimensional problems, later works [13]–[15] propose a methodology to apply it in three-dimensional cases.

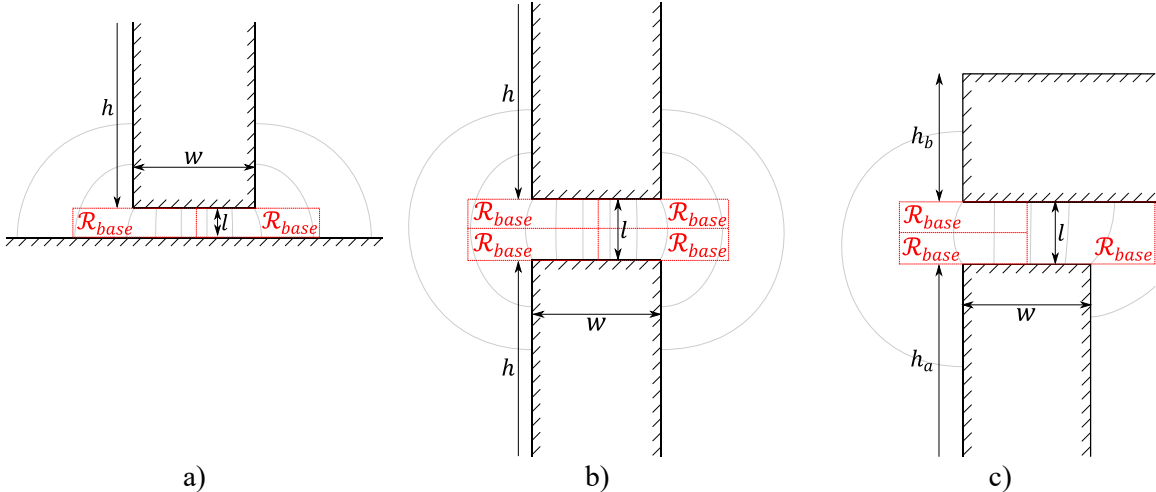


Fig. 3: a) Post-plate airgap made from two base reluctances in parallel, b) post-post airgap made from two post-plate airgaps in series (composed of four base reluctances), and c) edge airgap made from combining post-post and post-plate airgaps (composed of three base reluctances).

Using this base reluctance, both [12] and [13] identify different airgap types based on typical magnetic core assemblies. The nomenclature employed in this work follows the naming used in [12]. The common cases shown in Fig. 3 are analysed, were the equivalent reluctance expressions are based in the following geometrical assumptions:

- The post-plate airgap from Fig. 3a (type 3 according to [13]) is formed by two base reluctances in parallel, so that the two-dimensional reluctance can be directly obtained from (6). In [13] the two base reluctances are solved individually and added in parallel. Both approaches achieve the same result.

$$\mathcal{R}_{post-plate} = \mathcal{R}_{base} || \mathcal{R}_{base} = \frac{1}{\mu_0 \left[\frac{w}{l} + \frac{4}{\pi} \left(1 + \ln \frac{\pi h}{4l} \right) \right]} \quad (6)$$

- The post-post airgap from Fig. 3b (type 1 according to [13]) is made from two post-plate airgaps in series, so that the two-dimensional reluctance is simplified to (7). In [13] each reluctance is solved individually and then combined accordingly. The mathematical expressions obtained by both approaches are the same.

$$\mathcal{R}_{post-post} = \mathcal{R}_{post-plate} + \mathcal{R}_{post-plate} = \frac{1}{\mu_0 \left[\frac{w}{l} + \frac{2}{\pi} \left(1 + \ln \frac{\pi h}{2l} \right) \right]} \quad (7)$$

- The edge airgap from Fig. 3c (type 2 according to [13]) is made from half a post-post airgap in parallel with half a post-plate airgap, obtaining the expression (8). According to [12] the post-post reluctance can be solved by substituting h with the smallest post height between h_a and h_b . The technique proposed by [13] is slightly different, and the post-post reluctance is divided into three base reluctances, using the corresponding post height for each case instead of selecting the smallest value between h_a and h_b . Due to this, the edge airgap reluctances obtained from [12] and [13] differ slightly.

$$\mathcal{R}_{edge} = 2(\mathcal{R}_{post-post} || \mathcal{R}_{post-plate}) = \frac{1}{\mu_0 \left[\frac{w}{l} + \frac{1}{\pi} \left(1 + \ln \frac{\pi \min(h_a, h_b)}{2l} \right) + \frac{2}{\pi} \left(1 + \ln \frac{\pi h_a}{4l} \right) \right]} \quad (8)$$

The validity of these equations has been tested using a two-dimensional FEM simulations using FEMM [16], and mostly good agreements between analytical and FEM results have been obtained. Examples of various simulations are shown in Fig. 4, where a fine mesh area is defined around the airgap to obtain accurate results (shown as a rectangle). Furthermore, a comparison between the simulations and the analytical results is shown in Fig. 4. The post-plate and post-post airgaps maintain an error below 1.5% until $l > w/10$, while the edge airgap error for $l > w/10$ remains below 5%. For the edge airgap, the different approaches from [12] and [13] have been tested. The accuracy achieved by [12] is slightly worse than that obtained by applying [13], although the difference between these is less than 1% till $l > w/10$.

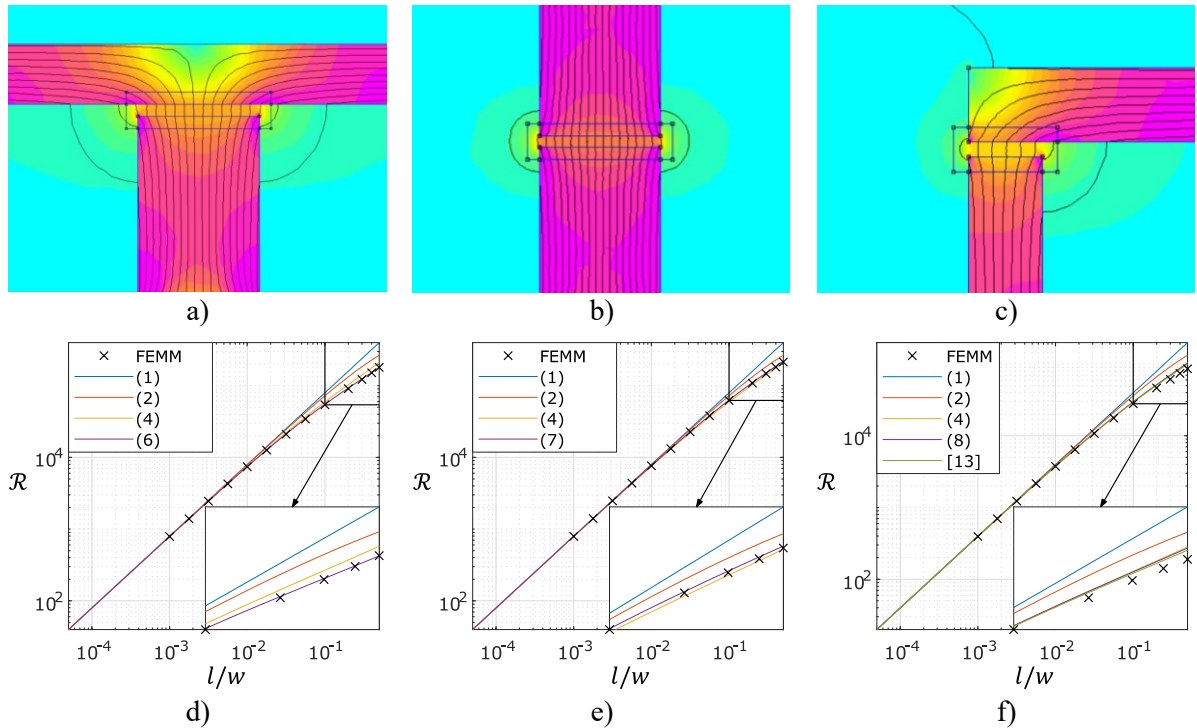
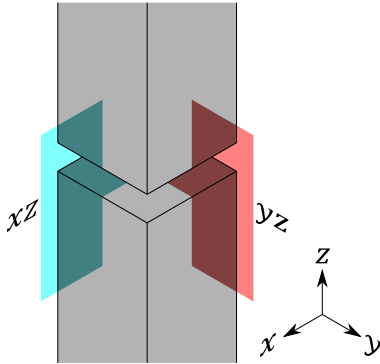


Fig. 4: FEM simulations of the magnetic flux density in a) post-plate, b) post-post and c) edge airgaps with the corresponding dimensions of an EE8020/EI8020 core with an airgap of 2 mm. The two dimensional reluctances obtained from the simulations and analytical approaches for various airgap lengths are shown in d), e) and f) respectively.

According to [13], it is possible to combine the two-dimensional reluctances to obtain the equivalent three-dimensional reluctance. To do so, it is necessary to obtain the fringing factors (σ) in the xz (9) and yz (10) planes shown in Fig. 5, which define how the two-dimensional airgap reluctances change due

to the fringing fields. Then, by applying both fringing factors to the three-dimensional reluctance without fringing field (1), the reluctance of the airgap with fringing field (11) is obtained.



$$\sigma_{xz} = \frac{\mathcal{R}_{xz}}{\frac{l}{\mu_0 w_x}} \quad (9)$$

$$\sigma_{yz} = \frac{\mathcal{R}_{yz}}{\frac{l}{\mu_0 w_y}} \quad (10)$$

$$\mathcal{R} = \sigma_{xz} \sigma_{yz} \frac{l}{\mu_0 w_x w_y} \quad (11)$$

Fig. 5: Representation of the xz and yz planes where the two-dimensional airgap reluctances are defined.

Comparisons with experimental results using EPCOS ferrite N27 EE55/28/21 cores and 1.0, 1.5 and 2.0 mm airgaps are presented in [13]. Due to the limited amount of experimental data (3 points), it is deemed necessary to perform more tests to verify the validity of the Schwarz-Christoffel transformation. Cosmo Ferrites CF139 EE5521, EE6527, and EE8020 cores have been tested [17]. The inductance has been measured using a BK Precision 891 LCR Meter at 10 kHz. The airgap reluctance is obtained by subtracting the effective reluctance of the core without airgap to the effective reluctance of the core with airgap. The results for these are shown in Tab. 1.

Tab. 1: Measured and calculated values of the airgap reluctance, as well as the difference between them, for three different EE cores and airgap lengths between 0.5 and 2 mm.

Core	l (mm)	Equation (1) (μH^{-1})	Equation (2) (μH^{-1})	Equation (4) (μH^{-1})	Approach [13] (μH^{-1})	Measured (μH^{-1})
EE5521	0.5	2.23 (+14.7%)	2.09 (+7.28%)	1.92 (-1.15%)	1.80 (-7.19%)	1.94
	1.0	4.46 (+37.0%)	3.91 (+20.2%)	3.50 (+7.43%)	3.14 (-3.61%)	3.26
	1.5	6.69 (+54.6%)	5.52 (+27.6%)	4.87 (+12.6%)	4.21 (-2.79%)	4.33
	2.0	8.91 (+66.2%)	6.94 (+29.3%)	6.11 (+13.8%)	5.10 (-4.96%)	5.37
	2.5	11.1 (+83.1%)	8.19 (+34.5%)	7.24 (+18.9%)	5.87 (-3.63%)	6.09
EE6527	0.5	1.47 (+10.5%)	1.40 (+4.61%)	1.30 (-2.57%)	1.23 (-7.78%)	1.33
	1.0	2.95 (+29.4%)	2.65 (+16.1%)	2.39 (+4.98%)	2.18 (-4.50%)	2.28
	1.5	4.42 (+44.8%)	3.77 (+23.5%)	3.36 (+10.0%)	2.95 (-3.24%)	3.05
	2.0	5.89 (+59.1%)	4.78 (+29.1%)	4.23 (+14.3%)	3.62 (-2.40%)	3.70
	2.5	7.37 (+70.9%)	5.69 (+32.1%)	5.04 (+17.0%)	4.19 (-2.74%)	4.31
EE8020	0.5	1.99 (+18.4%)	1.87 (+11.4%)	1.71 (+1.84%)	1.61 (-3.97%)	1.68
	1.0	3.98 (+40.0%)	3.53 (+24.1%)	3.10 (+9.13%)	2.80 (-1.54%)	2.84
	1.5	5.97 (+59.7%)	5.00 (+33.7%)	4.30 (+15.1%)	3.74 (+0.01%)	3.74
	2.0	7.96 (+74.9%)	6.30 (+38.5%)	5.37 (+18.1%)	5.51 (-0.87%)	4.55
	2.5	9.95 (+88.5%)	7.47 (+41.5%)	6.35 (+20.3%)	5.17 (-2.93%)	5.28

According to the new data presented, the Schwarz-Christoffel transformation based approach appears to be more accurate than the other techniques as the airgap length is increased. Note that only tests with EE cores are presented, thus only post-post reluctances (7) must be solved. Since the post-post reluctance is composed of two post-plate reluctances in series, there is reason to believe that (6) will achieve a similar accuracy, although the same cannot be said about (8). Curiously enough, for an airgap of 0.5 mm, the results from (4) are slightly more accurate than the Schwarz-Christoffel approach, although this changes as the airgap is increased. As the airgap length approaches zero, the different methods quickly converge, so similar accuracies can be expected for very low airgaps.

Application to other geometries

The previous data shows good agreements between experimental and analytical calculations based on the Schwarz-Christoffel transformation, but it has only been validated for EE cores. To ensure that the Schwarz-Christoffel transformation is valid to all common magnetic geometries, it is important to test other commonly employed core geometries, such as pot cores (Fig. 6). The cylindrical shape of these cores achieves a lower wire mean turn length, which reduces the copper losses. At the same time, the magnetic material surrounds the windings longer than in EE cores, which helps reduce EMI radiations.

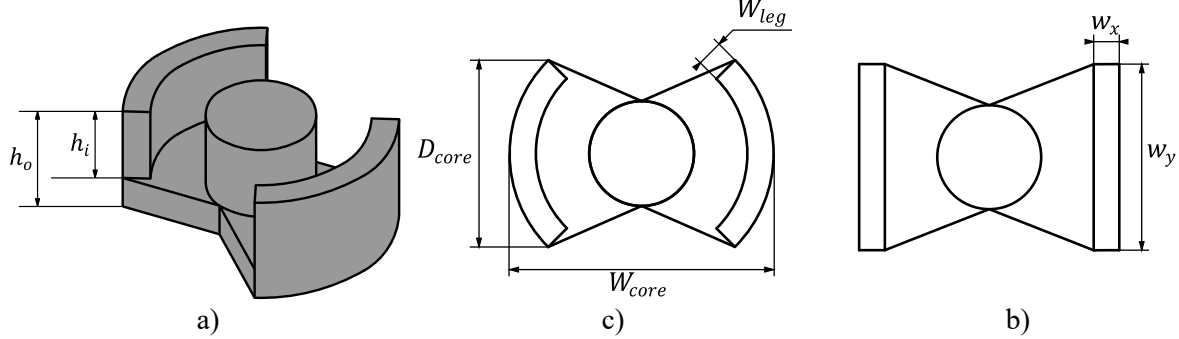


Fig. 6: a) Example of a PM pot core, b) the cross-section and b) geometrical transformation of the outer legs into rectangular sections.

Due to the cross-section shape of the pot cores, some geometrical changes are necessary to apply the Schwarz-Christoffel transformation. For the Cosmo Ferrites CF139 PM5039, PM6249, PM7459, and PM8770 cores tested [17], in the outer legs the value of \$w_x\$ is equal to the width of the leg (\$W_{leg}\$), but the value of \$w_y\$ must be derived from the pot core geometry. In this work, the transformation of the outer leg to a rectangular section is proposed, so that \$w_y\$ is then (12). The heights of the outer legs are different in the inside and outside of the core, which are defined as \$h_i\$ and \$h_o\$. In that case, the two dimensional reluctances of the outer legs are (13) and (14), and the approach from [13] can be used to obtain the three dimensional reluctance. The centre leg does not require any geometrical transformation, since as demonstrated in [13], the \$\sigma_{xz}\$ and \$\sigma_{yz}\$ factors are the same and represent the radial fringing factor (\$\sigma_r\$), so that the airgap reluctance is then (15).

$$w_y = (W_{core} - W_{leg}) \cos^{-1} \left(\frac{W_{core}}{D_{core}} \right) \quad (12)$$

$$\mathcal{R}_{xz} = \frac{1}{\mu_0 \left[\frac{w_x}{l} + \frac{2}{\pi} \left(1 + \ln \frac{\pi h_o}{2l} \right) \right]} \quad (13)$$

$$\mathcal{R}_{yz} = \frac{1}{\mu_0 \left[\frac{w_y}{l} + \frac{2}{\pi} \left(1 + \ln \frac{\pi \sqrt{h_i h_o}}{2l} \right) \right]} \quad (14)$$

$$\mathcal{R} = \sigma_r^2 \frac{l}{\mu_0 w_x^2 \pi / 4} \quad (15)$$

The results of the experimental tests for the four PM cores can be observed in Fig. 7. The data shows that the Schwarz-Christoffel transformation is the only approach capable of accurately estimating the impact of the airgap reluctance for long airgap lengths. It appears that the Schwarz-Christoffel transformation loses its accuracy at low airgap lengths, but there is not enough data to strongly validate this conclusion. Due to the tolerance of the gap spacers and the sensibility of the reluctance, it is not possible to test airgaps lower than 0.5 mm accurately.

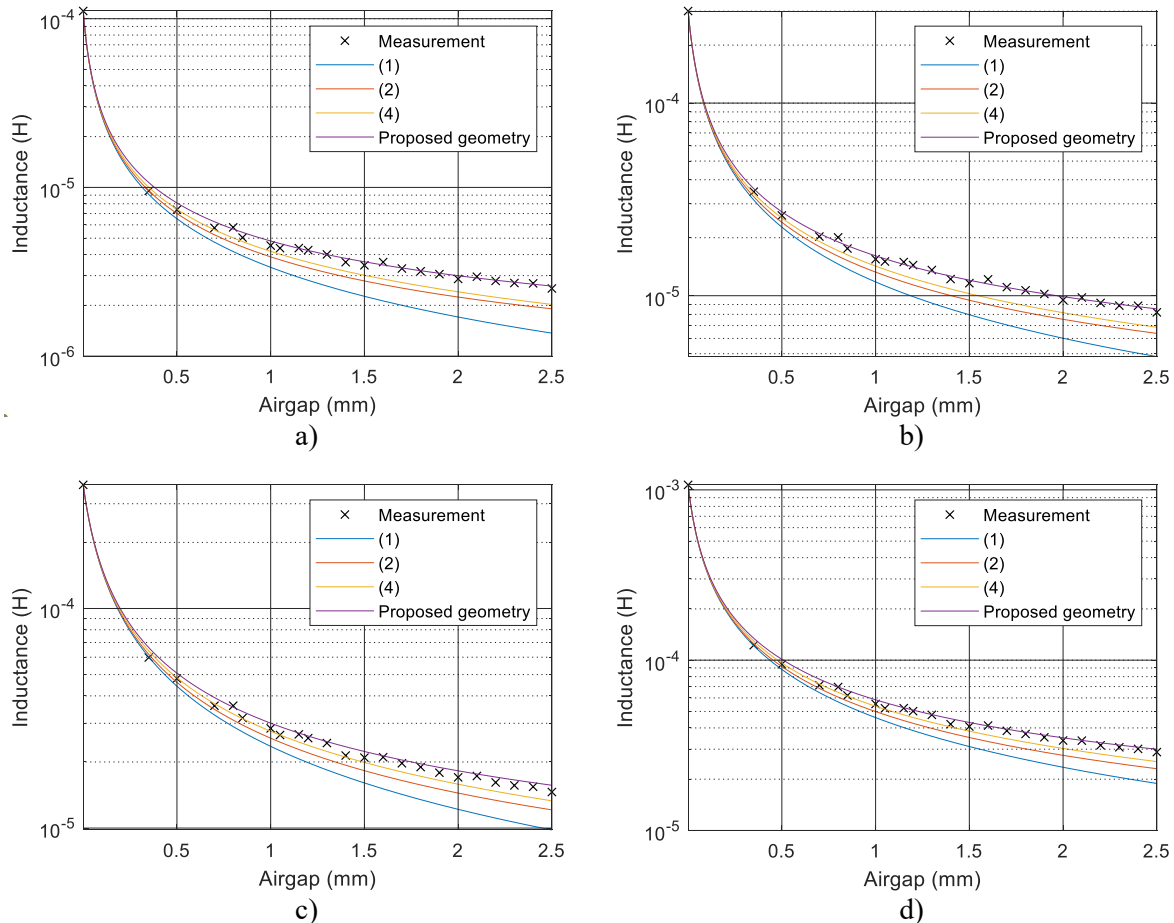


Fig. 7: Comparison of analytical and experimental results for a) PM5039, b) PM6249, c) PM7459 and d) PM8770 cores.

Conclusion

In this paper, various approaches to estimate the airgap reluctance of a magnetic core are studied, focusing on the effect of the fringing field. The Schwarz-Christoffel transformation based approach previously shown in [12], [13] is analysed and experimentally tested to solve the most common airgap geometries that appear in practical cases. The limited amount of experimental results presented in the literature is expanded for a larger airgap length range and more EE type cores. The analytical results are experimentally validated and reveal that the Schwarz-Christoffel approach is the only one capable of correctly assessing the reluctance for large airgap lengths.

The validity of the Schwarz-Christoffel transformation has also been tested in four PM pot cores, with airgap lengths ranging from 0.35 to 2.5 mm. A geometrical transformation to apply the Schwarz-Christoffel transformation to the cylindrical shape of these cores is proposed. According to the results, the Schwarz-Christoffel approach appears to be the most accurate at large airgap lengths, although its accuracy at low airgap lengths seems to be worse than in EE cores. Due to the tolerances of the gap spacers used, it has not been possible to analyse in detail the accuracy of these ranges, leaving this part of the study for future work.

References

- [1] G.F. Partridge B.Sc. F.Inst.P. (1936) LII. The inductance of iron-cored coils having an air gap , The London, Edinburgh, and Dublin Philosophical Magazine and Journal of Science, 22:148, 665-678, DOI: 10.1080/14786443608561717.

- [2] R. Lee, L. Wilson, and C. E. Carter, *Electronic Transformers and Circuits*. John Wiley & Sons Inc, 1988.
- [3] N. Mohan, T. M. Undeland, and W. P. Robbins, *Power Electronics: Converters, Applications, and Design*. John Wiley & Sons, Inc, 2002.
- [4] W. G. Hurley and W. H. Wölfle, *Transformers and Inductors for Power Electronics: Theory, Design and Applications*. John Wiley & Sons, Inc, 2013.
- [5] A. Ayachit and M. Kazimierczuk, “Sensitivity of Effective Relative Permeability for Gapped Magnetic Cores with Fringing Effect,” *IET Circuits, Devices & Systems*, vol. 11, no. 3, pp. 209–215, 2017.
- [6] W. T. McLyman, *Transformer and Inductor Design Handbook*. Marcel Dekker, Inc, 2004.
- [7] A. Van den Bossche and V. C. Valchev, *Inductors and Transformers for Power Electronics*. CRC Press, Taylor & Francis Group, 2005.
- [8] M. K. Kazimierczuk, *High-frequency magnetic components*. John Wiley & Sons, Inc, 2009.
- [9] R. Salas and J. Pleite, “Nonlinear Modeling of E-Type Ferrite Inductors Using Finite Element Analysis in 2D,” *Materials*, vol. 7, no. 8, pp. 5454–5469, 2014.
- [10] M. Beraki, J. P. F. Trovao, and P. Marina, “Characterization of Variable Inductors using Finite Element Analysis,” *Simulation Modelling Practice and Theory*, vol. 97, 2019.
- [11] S. Saeed, J. Garcia, M. S. Perdigão, V. S. Costa, B. Baptista, and A. M. S. Mendes, “Improved Inductance Calculation in Variable Power Inductors by Adjustment of the Reluctance Model Through Magnetic Path Analysis,” *IEEE Transactions on Industry Applications*, vol. 57, no. 2, pp. 1572–1587, 2021.
- [12] A. Balakrishnan, W. T. Joines, and T. G. Wilson, “Air-Gap Reluctance and Inductance Calculations for Magnetic Circuits Using a Schwarz–Christoffel Transformation,” *IEEE Transactions on Power Electronics*, vol. 12, no. 4, pp. 654–663, 1997.
- [13] J. Mühlethaler, J. W. Kolar, and A. Ecklebe, “A Novel Approach for 3D Air Gap Reluctance Calculations,” 2011.
- [14] Z. Yang, H. Suryanarayana, and F. Wang, “An Improved Design Method for Gapped Inductors Considering Fringing Effect,” 2019.
- [15] E. L. Barrio, A. Urtasun, A. Ursúa, L. Marroyo, and P. Sanchis, “Optimal DC gapped inductor design including high-frequency effects,” 2015.
- [16] D. C. Meeker, *Finite Element Method Magnetics, Version 4.2 (21Apr2019 Build)*, <https://www.femm.info>.
- [17] “COSMO FERRITES LIMITED.” <https://www.cosmoferrites.com/product-store/soft-ferrites> (accessed Mar. 30, 2022).